Dynamics of sediment flux to a bathyal continental margin section through the Paleocene-Eocene Thermal Maximum

Tom Dunkley Jones[1]*, Hayley R. Manners[2,3], Murray Hoggett[1], Sandra Kirtland Turner[4], Thomas Westerhold[5], Melanie J. Leng[6], Richard D. Pancost[7], Andy Ridgwell[4], Laia Alegret[8], Rob Duller[9], Stephen T. Grimes[2]

[1] School of Geography, Earth and Environmental Sciences, University of Birmingham, Edgbaston, Birmingham, B15 2TT, UK.
[2] School of Geography, Earth & Environmental Sciences, Plymouth University, Drake Circus, Plymouth, Devon, PL4 8AA, UK.
[3] School of Ocean and Earth Sciences, National Oceanography Centre, University of Southampton, Southampton, SO14 3ZH, UK.
[4] Department of Earth Sciences, University of California, Riverside, CA 92521, USA
[5] MARUM — Center for Marine Environmental Sciences, University of Bremen, Leobener Strasse, 28359 Bremen, Germany.
[6] NERC Isotope Geosciences Facilities, British Geological Survey, Nottingham NG12 5GG, UK & Centre for Environmental Geochemistry, University of Nottingham, Nottingham, NG7 2RD, UK.
[7] Organic Geochemistry Unit, The Cabot Institute, School of Chemistry, University of Bristol, Bristol, BS8 1TS, UK.
[8] Departamento de Ciencias de la Tierra & Instituto Universitario de Ciencias Ambientales, Universidad de Zaragoza, 50009 Zaragoza, Spain.
[9] Department of Earth, Ocean and Ecological Sciences, University of Liverpool, Liverpool, L69 3GP

Correspondence to: Tom Dunkley Jones (t.dunkleyjones@bham.ac.uk)

Abstract. The response of the Earth System to greenhouse-gas driven warming is of critical importance for the future trajectory of our planetary environment. Hypethermal events - past climate transients with significant global-scale warming - can provide insights into the nature and magnitude of these responses. The largest hyperthermal of the Cenozoic was the Paleocene-Eocene Thermal Maximum (PETM ~56 Ma). Here we present new high-resolution bulk sediment stable isotope and major element data for the classic PETM section at Zumaia, Spain. With this data we provide a new detailed stratigraphic correlation to the most complete marine and terrestrial PETM sections. With this new correlation and age model we are able to demonstrate that detrital sediment accumulation rates within this continental margin section increased more than four-fold during the PETM, representing a radical change in regional hydrology that drove dramatic increases in terrestrial to marine sediment flux. Most remarkable is that detrital accumulation rates remain high throughout the body of the PETM, and even reach peak values during the recovery phase of the characteristic PETM carbon isotope excursion (CIE). Using a series of Earth System Model inversions, we demonstrate that the silicate weathering feedback alone is insufficient to recover the PETM CIE, and that active organic carbon burial is required to match the observed dynamics of the CIE. Further, that the period of maximum organic carbon sequestration coincides with the peak in detrital accumulation rates observed at Zumaia. Based on these results, we

hypothesize that hydrological controls on sediment dynamics may contribute to the rapid climate and CIE recovery from peak-PETM conditions.

1 Introduction

The PETM is a marked interval of climate warming (Dunkley Jones et al., 2013), shoaling of oceanic
5 carbonate saturation horizons (Zachos et al., 2005) and a large global negative Carbon Isotope Excursion (CIE) in all rapidly exchangeable marine and terrestrial carbon reservoirs (McInerney and Wing, 2011). The most consistent explanation for these coupled perturbations is the release of carbon from a large shallow lithospheric reservoir, with a depleted carbon isotopic ($\delta^{13}C$) signature ($\sim$ –20 to – 60 ‰), on a multi-millenial timescale (Bowen et al., 2015; Dickens et al., 1995; Gutjahr et al., 2017;
10 Kirtland Turner and Ridgwell, 2016; Zeebe et al., 2016). Although there is still no confidence on the identity of such a large (>4000 Pg C) and unstable carbon reservoir, its release and oxidation within the ocean-atmosphere system caused rising atmospheric CO_2 concentrations, warming and a range of Earth System perturbations associated with pronounced global warming (Sluijs et al., 2007).

15 Although considerable attention has been paid to constraining the rates of carbon release, based on deep-ocean carbonate dissolution (Panchuk et al., 2008; Zachos et al., 2005; Zeebe et al., 2009), rates of warming (Meissner et al., 2014; Zeebe et al., 2016), carbon isotope profiles (Bowen et al., 2015; Kirtland Turner and Ridgwell, 2016) and surface ocean pH (Gutjahr et al., 2017) the mechanisms responsible for both the climatic and isotope recovery at the end of this transient event are still not well
20 constrained (Bowen and Zachos, 2010). The timescales of silicate weathering and carbonate burial ($\sim$100-200 ka) are suggested to be too long to drive the main phase of CIE recovery, which the best records available to date indicate is an order of magnitude faster ($\sim$10-20 ka) (Bowen and Zachos, 2010). However, observed patterns of enhanced carbonate and possibly biogenic silica deposition in the deep-ocean through the PETM recovery phase are interpreted as the signature of a silicate weathering-
25 driven recovery (Penman, 2016; Penman et al., 2016). The alternative mechanism for carbon removal is the substantial burial of organic carbon within either terrestrial or marine sedimentary systems (Bowen and Zachos, 2010). One means of increasing global organic carbon burial rates is through enhanced sedimentation rates on continental margins, which might contribute significantly to C_{org} burial rates with little or no rise in measured total weight percent organic carbon content of sediments (Sluijs et al.,
30 2014). There is also direct evidence for substantial increases in the organic carbon content of syn-PETM marine sediments in the eastern Tethys, associated with increased terrestrial to marine weathering fluxes and reduced seawater oxygenation (Carmichael et al., 2017; Gavrilov et al., 1997).

If organic carbon burial does drive recovery from the PETM, there is no explanation for the temporal
35 offset between increased sedimentation rates and organic carbon burial during the body of the PETM (John et al., 2008) – when models indicate no or little carbon removal from the systems – and the major phase of carbon burial required for the CIE recovery at the end of the event. Models that include a continued leakage of carbon to maintain a prolonged CIE provide a mechanism to delay recovery (Penman et al., 2016; Zeebe et al., 2009), but this delay only exacerbates the mismatch between the

observed fast recovery and the timescales of silicate weathering-driven carbon drawdown (Penman et al., 2016). As yet, there is no satisfactory model to explain the timing of the large-scale carbon drawdown required to drive the rapid CIE recovery phase ~100 ka after the onset of the PETM (Bowen and Zachos, 2010). Understanding the ultimate fate of thousands of petagrams of "excess" carbon

5 injected into the ocean-atmosphere system during the PETM has profound implications for understanding the behaviour of the Earth's climate future over the coming millennia. Here, we present new high-resolution bulk carbonate isotopic analyses, calcium carbonate and organic carbon contents and bulk sediment elemental data from the Iberian upper continental slope (~1000m paleo-water depth), to address the linkage between climatic controls on sedimentation rates and carbon drawdown. We

10 reference this data within a new best-fit age model, constrained by detailed stratigraphic correlations to the most complete terrestrial and marine PETM successions.

2 Location and Methods

Our studied PETM section is located at the Itzurun beach-front of the town of Zumaia, northern Spain (Figure 1; N 043°18´4.5", W 002°15´31.2"). Situated within the deep-basin of the Pyrenean Gulf, it is

15 the deep-water end of a sediment distribution system that has been mapped in detail over the past two decades (see references and summary within Pujalte et al., 2015). Logged sections span terrestrial alluvial fans and plains, shallow shelf carbonates, incised channel distribution systems and a deep-water basin (Pujalte et al., 2015 and references therein). Within this, the Zumaia section is regarded as the most complete and representative end member of the deep-water depositional system, recording the

20 distal deposition of fluvial-derived fine grained sediment plumes (Pujalte et al., 2015) at middle-lower bathyal (1000 m) paleodepths (Alegret et al., 2009).

The Zumaia section is a classic PETM locality and the subject of a series of bio-, magneto-, chemo-, and lithostratigraphic studies (Alegret et al., 2018; Alegret et al., 2009; Baceta et al., 2000; Bernaola et

25 al., 2007; Canudo et al., 1995; Dinarès-Turell et al., 2007; Dinarès-Turell et al., 2002; Manners et al., 2013; Schmitz et al., 1997; Schmitz et al., 2001; Storme et al., 2012). The aim of this study is to build on the existing detailed depositional framework developed for the region, and to use the Zumaia section as a key recorder of the temporal patterns of climate-driven sediment flux from terrestrial systems to the deep ocean during the PETM. To do this we sought to substantially increase the resolution of existing

30 bulk carbonate isotope records and supplement these by high-resolution bulk sediment compositional analyses by X-ray Fluorescence (XRF). This approach is consistent with a progressive shift in PETM studies, from broad characterization of the CIE as a marker of the event within wider Paleogene stratigraphy, to a focus on the millennial-scale dynamics of the carbon cycle, climate and other Earth System properties within the PETM itself (Bowen et al., 2015; Zeebe et al., 2016). For this study we

35 took a total of 248 small "thumbnail" 1cc bulk sediment samples at ~3 to 5cm resolution from ~4.3 m below to ~8.2 m above the onset of the characteristic "siliciclastic unit" that marks the body of the PETM at this location. The zero reference point for all sampling is taken at the top of the prominent limestone bed, located ~0.3 m below the base of the SU. In between the limestone and the SU is a 0.3 m thick greenish-grey marl unit, which is distinct from both the limestone / marl units found above and

below the SU and the typically red-brown clays and marly clays of the SU itself. The section was logged in detail, and integrated with the existing stratigraphic framework for the site (Figure 2).

All samples were analysed for bulk sediment elemental composition by X-ray Fluoresence (XRF) using dried, powered sediment, mounted in wax pellets. Pellets were analysed with a Bruker S8 tiger X-Ray Fluorescence (XRF) Spectrometer with 8-minute analysis time, at the University of Birmingham (UoB). CaO concentrations from XRF analyses were converted into high-resolution estimates of weight percent $CaCO_3$ using a calibration set of 25 discrete calcium carbonate measurements. Weight percent $CaCO_3$ contents were determined at UoB, based on inorganic carbon contents measured by CO_2 generation with phosphoric acid reaction within a 200ºC furnace using a Shimadzu TOC-V carbon analyser. Detrital MARs were estimated assuming that both detrital and carbonate fractions had an estimated dry bulk density of 1.8 g cm^{-3}. Organic carbon MARs were calculated following Willmott et al. (2009).

A subset of 129 thumbnail samples were also analyzed for the stable isotope composition ($\delta^{13}C_{carb}$ and $\delta^{18}O_{carb}$) of bulk carbonates at the NERC Isotope Geosciences Laboratory (NIGL, Keyworth, Nottingham). Sample material was powdered to yield CO_2 from the equivalent of 10 mg of 100% calcite and reacted with anhydrous phosphoric acid *in vacuo* overnight at a constant 25°C. Liberated CO_2 was separated from water vapour under vacuum and collected for analysis. Measurements were made on a VG Optima mass spectrometer (standard reproducibility of $< \pm 0.1$‰). All data are on the VPDB scale. An additional 67 bulk samples were analysed for total organic carbon content at NIGL using a Carlo Erba 1500 elemental analyser with acetanilide used as the calibration standard. Replicate analyses indicated a precision of ±0.1 wt% in well-mixed samples (1 Standard Deviation, SD).

3. Stratigraphy and Age Model

3.1 Carbon Isotope Stratigraphy
The new high-resolution bulk carbonate isotope stratigraphy presented here is consistent with previous studies of the Zumaia section, in particular the isotopic data of Schmitz et al. (1997). The capacity for the analyses of low weight carbonate samples at NIGL has, however, provided substantial additional data within the critical phase of most rapid change at the PETM onset, between ~0.3 and 0.7 m. This new data provides information about subtle lead/lag relationships between lithological change at the base of the SU, sediment carbonate content, the CIE and benthic foraminifera community change and extinction (Alegret et al., 2018). Although there is a clear negative $\delta^{13}C$ shift of ~ 1 ‰ between the prominent limestone unit (-0.7 to 0 m) and the 0.3 m thick marl unit (0 to 0.3 m) that immediately underlies the SU, this change, and the absolute $\delta^{13}C$ values concerned, are all within the background variations in $\delta^{13}C$ seen in the marl / limestone couplets of the latest Paleocene (e.g. from -4.0 to -1.0 m). For example, the carbonate $\delta^{13}C$ values of ~0 ‰ within the "precursor" marl unit (0 to 0.3 m) are close to the average value for the latest Paleocene succession analyzed in this study. On this basis, we take a conservative approach and do not identify this $\delta^{13}C$ shift as related to the onset of the main phase of the PETM. This is not to say that there are not significant environmental perturbations through the limestone and precursor marl intervals. There is evidence for an early shift in both benthic (Alegret et

al., 2018) and planktonic foraminiferal assemablages within this marl unit (Schmitz et al. 1997). Further the distinct precursor limestone bed is itself an unusual feature within the typically thinner, and lower CaCO$_3$ "limestone-marl" couplets of the latest Paleocene. The nature of any such precursor environmental changes are beyond the scope of this study, but they do underline the potentially great importance and utility of the Zumaia section, because, unlike many deep-ocean sites, it appears to be more continuous and expanded across the onset of the PETM.

Here, we place the base of the CIE at 0.30 m. The δ^{13}C shift between 0.25 m (0.01 ‰) and 0.30 m (-0.28 ‰) is the start of the consistent negative deviation in δ^{13}C values that continues through the base of the SU. This level is also the point of lithological change between the precursor marl and the base of the SU. The largest negative step in δ^{13}C - from -0.8 to -3.6 ‰ - is recorded between samples 0.34 and 0.38 m with a further decline to values of -4.0 ‰ or lower above 0.5 m (Figure 2). The total CIE is more than ~3.7 ‰ (Figure 2). We note that there is a slight lag between the onset of the CIE and the corresponding decline in calcium carbonate contents. Carbonate contents are stable between 0.25 and 0.30 m, at ~44 wt%, but then drop rapidly across successive samples to 26 wt% (0.34 m) and then 7 wt% (0.38 m). The placement of the onset of the CIE at 0.30 m also agrees well with the main phase of the Benthic Foraminifera Extinction event (BEE), which was placed at ~0.3 m in the original study of Schmitz et al. (1997) as well as in detailed analyses of foraminiferal turnover (Alegret et al., 2018; Alegret et al., 2009). A gradual but rapid disappearance of benthic foraminifera is recorded through the precursor marls (0 to 0.30 m), but the main phase of the BEE coincides with the onset of the negative CIE at ~0.3 m (Alegret et al., 2018)

Although the marked increase in sedimentation rates at the onset of the PETM limits the effects of any carbonate burndown on the δ^{13}C$_{carb}$ record across the onset, δ^{13}C$_{carb}$ data appear to diverge from the typical PETM CIE profile between ~0.7 to 2.8m. Here, δ^{13}C$_{carb}$ values return to higher values, of ~ –3‰, which lie between those of the peak CIE and pre-excursion values (Figure 2). This is attributed to the increased relative contribution of reworked detrital carbonates, as evidenced by the presence of Cretaceous nannofossils (Dunkley Jones, pers. obs.), during periods of very low autochthonous carbonate flux. This is supported by the return of δ^{13}C$_{carb}$ to near peak-excursion values once carbonate contents increase above 2.8m. Above this level, there is a CIE recovery phase similar to other high-resolution records from terrestrial section and the deep ocean (e.g. Bowen et al., 2015; Zachos et al., 2005; Figure 2).

In order to develop a robust age model for the Zumaia section, we used our new high-resolution stable isotope stratigraphy, together with the established cyclostratigraphy for the Zumaia section, based on precession-paced lithological cycles (Dinarès-Turell et al., 2003; Westerhold et al., 2008). This combination of carbon isotope and cyclostratigraphy provided multiple direct stratigraphic ties to existing deep-ocean and terrestrial (Bowen et al., 2015; Röhl et al., 2007; Westerhold et al., 2018) locations. These tie points include precession cycles -9 to -14 below the onset of the PETM, and cycles 6 to 14 above the onset of the PETM, as well as the CIE onset and marked inflexion point in δ^{13}C during the recovery phase (~55.81 Ma). In the latest Paleocene, distinct marl/limestone couplets are lost with the deposition of more continuous higher carbonate lithologies between ~ -1.0 and 0 m, including

the distinct marker limestone bed. This high carbonate interval may be due to clastic sediment starvation, and has previously been associated with the base of a transgressive systems tract (Storme et al., 2012). The new bulk sediment chemistry presented here is also unable to clearly identify cycles within this interval, but interpolations to Chron 25n and biostratigraphic correlations between Zumaia

5   and deep ocean sections, would suggest that this high carbonate interval is relatively condensed. In this study, we associate the first clear limestone/marl couplet beneath this high carbonate interval (marl between -1.4 and -1.8 m) with the 9th precession cycle below the onset of the CIE. Above the SU, two prominent thicker carbonate beds are correlated with the 100 ka eccentricity minima of Westerhold *et al*. (2007; precession cycles 6/7 and 11), which is supported by the placement of the Last Rare

10   Occurrence of the calcareous nannofossil genus *Fasciculithus* at 8.7 m (Baceta et al., 2006; confirmed by Dunkley Jones, pers. obs.), between cycles 15 and 16, which is consistent with Forada section and ODP Site 690 (Röhl et al., 2007).

15   **3.2 Sedimentary Cycles through the PETM**

Our new bulk sediment elemental analyses show the same precession-paced lithological cycles above and below the main body of the PETM (Dinarès-Turell et al., 2003; Westerhold et al., 2008; Westerhold et al., 2018). This same prominent cyclicity is resolved in carbonate content but also in SiO_2 and Si/Fe

20   ratios both below and above the SU (Figure 3). In addition to these already established precession cycles, we note, for the first time, a prominent variation in Si/Fe ratios through through the SU itself. This takes the form of 10 cycles in Si/Fe between the CIE onset and the $\delta^{13}C$ inflection point F of Röhl et al. (2007; Figure 3). With a total CIE duration of 90-167 ka (Murphy et al., 2010; Röhl et al., 2007) this variability is on the half-precession timescale (10*10.5=105 ka) of a strikingly similar nature to

25   variations observed in terrestrial palaeosol successions from the Bighorn Basin (Abdul Aziz et al., 2008; Westerhold et al., 2018). This variability is most likely linked to catchment hydrology (e.g. Abdul Aziz et al., 2008), resulting from the interference of both northern and southern hemisphere precession signals within tropical hydroclimates (Short et al., 1991). This is consistent with a strong hydroclimate control on sediment erosion and transport in the Tremp-Graus terrestrial basins during the PETM

30   (Pujalte et al., 2015; Schmitz and Pujalte, 2007).

Spectral analysis of the new high-resolution Zumaia Si/Fe records resolve significant power at frequencies of ~2.2 cycles m^{-1} (~0.45 m period) and 0.7 cycles m^{-1} (~1.4 m period) (Figure 4). This double peak in power spectra is unlikely to be due to a simple step-change in sedimentation rates at the

35   onset of the PETM conditions – with an associated shift in the frequency of precession signals in the depth domain - as power is resolved at both frequencies within the body of the PETM where sedimentation rates are relatively stable (Figure 3). In our preferred analysis, we use these ten intra-PETM Si/Fe cycles to provide additional age constraints through the PETM at Zumaia. The use of these cycles does not impact the wider detailed correlations to other locations based on carbon isotope

40   stratigraphy and cyclostratigraphy outside of the body of the PETM as presented above. We believe these correlations are robust and provide an excellent context for interpreting the Zumaia record. The presence of distinct variability in Si/Fe ratios though the body of the SU at Zumaia simple provides

additional, fine-scale lithological and bulk rock geochemical data for an otherwise poorly resolved interval. It is our contention that these cycles represent primary bulk rock geochemistry, and follow established practice in the use of Fe counts from XRF data, which are the primary means of determining cyclostratigraphic models within Paleogene successions (e.g. Röhl et al., 2007; Westerhold et al., 2007; Westerhold et al., 2014; Westerhold et al., 2008; Westerhold et al., 2018; Zachos et al., 2010).

Although other sections within the Basque Basin show distinct lithological variability through the PETM, including turbidite deposition at the shallower-water section of Ermua (Schmitz et al., 2001) and the development of large deep-water distribution channels (Pujalte et al., 2015), no evidence for either turbidite deposition or any significant unconformity has been reported for the section at Zumaia. Indeed, "*the Zumaia section is the most complete and representative section of the deep-water Basque Basin across the P-E interval*" (page 1655; Pujalte et al., 2015).Throughout the main phase of the PETM, sediments of the Zumaia section are dominated by fine-grained sediments, with the <28 μm fraction typically contributing 99 %, or more, of sediment volume during the SU (Schmitz et al., 2001). This is consistent with the remarkable absence of any turbidite deposition during the PETM phase at Zumaia (Clare et al., 2015). Together, all available evidence indicates the continuous and relatively uniform deposition of fine-grained hemi-pelagic clays through the PETM at Zumaia. It is this feature that makes the Zumaia section an important location for the detailed study of the dynamics of biotic and geochemical perturbations through the PETM.

4 Calcium Carbonate and Detrital Sediment Mass Accumulation Rates

Based on our age model and estimated weight % $CaCO_3$, we estimate calcium carbonate, total organic carbon (TOC) and detrital mass accumulation rates (MAR) throughout the study interval (Figures 5 and 6). Carbonate MAR closely follows weight % $CaCO_3$, with a marked decline during the body of the SU. The records do, however, diverge in two key intervals: first during the distinct limestone bed below the onset of the PETM, between ~ -0.8 and 0 m (~56.03 to 55.95 Ma), and then in the later stage of the CIE recovery between ~4.4 and 4.7m (55.82 to 55.81 Ma) (Figures 5 and 6). In the first of these, the distinct high carbonate content of the limestone unit is weakly represented in carbonate MAR, indicating that this is the result of clastic sediment starvation, rather than increased carbonate production. The second horizon occurs during the CIE recovery phase, when carbonate MARs nearly treble compared to pre-PETM values before stabilizing at levels ~50% higher than pre-PETM conditions during the post-PETM phase above 4.7 m (~55.81 Ma). This persistent increase in carbonate MARs above the PETM is reflected in consistently higher carbonate contents ($CaCO_3$ wt %) of sediments above the PETM than those in the latest Paleocene. This is clear evidence for significantly increased carbonate accumulation rates post-PETM, even in relatively shallow (~1000m) supra-lysoclinal depths on the continental margins. The rate and timing of this recovery in carbonate MARs is also remarkable, with not only recovery to background levels, but also this switch to significantly elevated MARs all occurring within the main phase of the CIE recovery in less than 20 ka (Figure 6).

The mass accumulation rate of non-carbonate components is here considered equal to the detrital MAR, in the absence of any significant contribution of biogenic silica. Before the CIE, the detrital MARs are relatively low, fluctuating around 2 g cm^{-2} ka^{-1}, with a further decline during the precursor limestone unit (–0.8 to 0 m). During the onset of the PETM (0.3 – 1.5 m) detrital fluxes increase dramatically, to between three and four times pre-PETM levels. Within the peak-PETM (1.5-1.7 m; ~55.88 to 55.85 Ma), detrital flux declines slightly and shows variability on similar timescales to Si/Fe ratios. It then increases markedly towards the end of the peak-PETM interval, above 3.7 m (~55.85 Ma), and reaches peak values for the whole PETM during the main phase of the δ^{13}C recovery interval (3.7 – 4.2 m; ~55.83 to 55.82 Ma). Both detrital and carbonate MAR increase, to peak values for the whole PETM, during the main interval of CIE recovery, with detrital MARs peaking first, followed by carbonate MARs. We note that these high detrital mass accumulations rates during the body of the PETM do not coincide with a noticeable increase in grain size, with sediments dominated by clay-grade material throughout. This is consistent with the marked absence of coarser grained turbidite deposition during the PETM within the Zumaia section (Clare et al., 2015), although major increases in coarse grained siliciclastic deposits during the PETM are recorded within deep-water channels within the basin (Pujalte et al., 2015). Total organic carbon MARs are relatively stable before the onset of the event, at ~0.01 g cm^{-2} ka^{-1}. At the onset of the PETM there is an increase in TOC MARs, but this lags the CIE onset by ~20 ka (Figure 6). During the body of the PETM there are distinct peaks in TOC MARs at ~55.90 Ma and ~55.85 Ma, but in general values remain between 0.015 and 0.02 g cm^{-2} ka^{-1}. Coincident with recovery the CIE recovery phase, TOC MARs increase again to over ~0.02 g cm^{-2} ka^{-1} between 55.83 and 55.81 Ma.

5 Inverse Modelling the Zumaia CIE and the PETM carbon source

To constrain the rates of carbon input and sequestration through the onset and termination of the PETM, based on the CIE profile and cyclostratigraphy from Zumaia, we undertook a series of PETM simulations using the late Paleocene-early Eocene configuration of the cGENIE Earth System Model. This includes a 3-D dynamic ocean model, 2D energy balance atmospheric model, and a representation of marine biogeochemical cycling plus the preservation of carbonates in deep-sea sediments (Ridgwell and Schmidt, 2010). We also include a 0-D (global average) temperature-dependent terrestrial weathering feedback as described in (Colbourn et al., 2013). We follow a two-part spin-up procedure, first for 20 ka as a 'closed' system (i.e. weathering exactly balancing sedimentation) and with atmospheric CO$_2$ set to 834 ppm with a δ^{13}C of -4.9‰. A further 250 ka 'open system' spin-up with temperature-dependent weathering feedbacks enabled and input of CO$_2$ via volcanic outgassing (Colbourn et al., 2013) was used to bring the geological ^{13}C cycle to steady state. In this, the specified detrital flux to the sediments (non-carbonate) (0.18 g cm^{-2} ka^{-1}), the rain ratio of carbonate to particulate organic carbon (0.2), and the global average concentrations of Mg^{2+} and Ca^{2+} (29.89 and 18.22 mmol kg^{-1}, respectively) and alkalinity (1975 μmol kg^{-1}) were selected to give an average global mean sedimentary carbonate preservation of 46.75%, comparable with late Paleocene estimates (Panchuk et al., 2008).

Four inversion experiments were undertaken, all forced with carbon (CO_2) inputs to the atmosphere such that the $\delta^{13}C$ of surface ocean dissolved inorganic carbon (DIC) followed a prescribed inversion target taken from the Zumaia $\delta^{13}C$ record, adjusted to the initial cGENIE average surface ocean DIC $\delta^{13}C$ of +2.7‰. Within the very low carbonate interval, where the primary signals appear to be lost due to the disproportionate influence of non-autochthonous carbonates, the $\delta^{13}C$ target curve was linearly interpolated between the data points at ~19 and 78 ka. Experiments included variation in the isotope composition of the source (–60‰ and –22‰) and CIE recovery driven by silicate weathering only and with active carbon removal to match the CIE profile (Table 1). In order to directly compare modelled and observed carbonate contents, all experiments also include the temporally varying observed changes in detrital fluxes within the sediment model at the model grid-box corresponding to the paleolocation of Zumaia only.

Net input fluxes depend on the $\delta^{13}C$ composition of the source (Table 1), with smaller carbon inputs required for a source with a more negative isotope composition. Total carbon inputs are also slightly larger where no removal fluxes are allowed (Experiment 1). In all experiments, the majority of C input occurs in the first 20 ka with a low rate of C input (<0.05 Pg C yr-1) required to maintain low isotope values until 78 ka. Total modelled C input is broadly comparable to previous model-based estimates constrained by deep-ocean carbonate dissolution that exceed ~4000 Pg C (Bowen et al., 2015; Cui et al., 2011; Gutjahr et al., 2017; Panchuk et al., 2008). In this case the lower bound of carbon input (4154 PgC) is generated by an inversion of the CIE isotopic profile assuming a pure biogenic methane carbon source with isotope composition of –60‰. As an independent test of the reliability of these simulations, in terms of the estimated CIE magnitude and temporal dynamics, the modelled atmospheric $\delta^{13}C$ excursion is compared to the best available terrestrial record of the CIE, from soil carbonates of the Bighorn Basin (Figure 7; Bowen et al., 2015). There is a strong correspondence between the two, in the shape of the onset and recovery, the magnitude of the CIE and the overall duration of the event. Although these model runs have no independent second constraint on the carbon cycle perturbation through the PETM – for example a measure of surface ocean pH change (Gutjahr et al., 2017) or deep ocean carbonate saturation state (Panchuk et al., 2008; Zeebe et al., 2009) – model simulations with a mixed source input with $\delta^{13}C$ of -22 ‰ are close in total mass input across the PETM onset (11,316 Pg C) to the preferred simulations of Gutjahr et al. (2017; ~10,200 Pg C), which are constrained by surface ocean pH changes. The combination of these two records – pH from DSDP Site 401 and the CIE dynamics from Zumaia – is, however, informative. Total carbon input masses, constrained by the most detailed surface ocean pH records of the PETM available to date, are modelled to be >10,000 Pg C (Gutjahr et al., 2017), but the dynamics of this release must be considerably quicker than assumed within the deep-ocean records recovered from Site DSDP Site 401, in order to satisfy the rate of CIE onset observed at Zumaia, which is ~3.3 ‰ over less than 5 ka. We argue that this CIE onset rate is robust, given that it is observed in both terrestrial (Bowen et al., 2015) and marine (this study) sections where the onset of the CIE is expanded and set within a robust intra-PETM cyclostratigraphic age model. The CIE recorded at Zumaia, and within the Big Horn Basin (Bowen et al., 2015), of 4 ‰ or more, is also greater than that assumed in the favoured model simulations of Gutjahr et al. (2017) of 2.6 ‰, and is closer to their alternate run assuming a CIE of ~4 ‰, which reconstructs a source carbon source with a $\delta^{13}C$ composition of ~ -17 ‰. Both these aspects of the Zumaia record – a CIE onset less

than 5 ka, and a CIE with magnitude ~4 ‰ or more – requires the rapid release of carbon from a source that is more isotopically-depleted than volcanic CO_2. Whether thermogenic methane generated by sill intrusion during the onset phase of the NAIP (Svensen et al., 2004) can meet the emission rates and carbon isotopic compositions required to generate the early stages of the CIE is yet to be resolved.

6 Carbon Removal During the PETM Recovery

Two fundamental unknowns remain about the recovery phase of the PETM: first, what is the ultimate sink of thousands of petagrams of carbon when added to the ocean-atmopshere system as CO_2?; and, second, what controls the temporal dynamics of carbon flux into this sink, and thence controls the timing of the relatively rapid CIE and PETM climate recovery? The combination of the age-constrained CIE records from Zumaia, the inverse Earth System modelling of this CIE and the general excellent agreement between the atmospheric CIE generated in these simulations with independent records from the terrestrial realm (Figure 7; Bowen et al., 2015), provide new insights into these key questions. In simulations without active carbon removal, the only process restoring atmospheric pCO_2 to pre-CIE levels is the silicate weathering feedback, where net removal depends on the size of the carbon input and associated temperature change. This "weathering only" experiment fails to match the observed CIE recovery, with minimal recovery of atmospheric CO_2 $\delta^{13}C$ even when a significant mass of carbon has been removed from the atmosphere (Figure 7). This is due to the isotopic imbalance between the ultimate carbon sink in this case – marine carbonates (-1 to 4‰) – compared to the carbon source (–22 or –60 ‰). With the weathering feedback only, the rate of removal of carbon from the atmosphere (Figure 7), and associated climate recovery, also occurs on timescales significantly longer (> 100 ka) than indicated by climate proxy data, where temperatures are closely coupled to the recovery of the CIE (Dunkley Jones et al., 2013). The configuration of the silicate weathering feedback within the model is thus an insufficient driver of PETM recovery on two counts: first its inability to drive recovery in the carbon isotopic composition of the exogenic carbon reservoir, and second, in its inability to match the rate of recovery of the climate system at the end of the PETM. The Zumaia record also provides evidence for a rapid climate transition at the end of the PETM, independent of carbon-cycle system parameters (e.g. $\delta^{13}C$ and $CaCO_3$ accumulation), in the observed rapid switch back to pre-PETM detrital fluxes during the recovery phase. This implies a rapid climate recovery - back to a hydrological and erosive system similar to pre-event conditions - that is very closely coupled to the CIE recovery (Figure 6).

To correctly simulate both the CIE and the climate system (temperature, hydrology) recovery rates, the active removal of large masses of isotopically light carbon is required during the PETM recovery phase. Simple isotope mass balance requirements require a greater mass of carbon to be removed than was first released, if the isotopic composition of the sink is more positive (organic carbon -22 %) than that of the source (biogenic methane -60 %). In these methane input / organic carbon burial simulations (Experiment 4), the required excess carbon removal (removal mass minus input mass) causes a remnant post-event climate forcing, with an ~60% decline in post-PETM atmospheric CO_2 levels relative to pre-PETM conditions (Figure 7), and a global mean surface temperature reduction of ~ 4ºC. At present

there is no evidence for such a post-PETM cooling, which would suggest that the source and sink terms are relatively close in their isotopic compositions and precludes a biogenic methane input / organic carbon burial scenario.

5   The simulations that best match the constraints of the CIE and PETM recovery are those with the active removal of carbon, focused on the main phase of the CIE recovery, and with an isotopic composition close to that of the original carbon source. The failure of the silicate weathering feedback alone to match the rate and magnitude of CIE recovery is similar to the recent inverse modelling by Gutjahr et al. (2017), where 2,500 Pg of carbon removal, with isotopic composition of -30.5 ‰, was required to

10 match the CIE. The larger masses of carbon removal required in the simulations presented here are due to the smaller magnitude CIE recorded at DSDP Site 401, the target CIE curve for Gutjahr et al. (2017), and the isotopically lighter composition of the carbon sink used (-30.5 ‰) by Gutjahr et al. (2017) compared to this study (-22 ‰).

15 The question remains as to what is the driver of enhanced carbon burial during the CIE recovery interval? In the Zumaia records it is notable that exactly this interval – the CIE recovery phase – is directly coupled with maxima in total sedimentation rates and detrital mass accumulation rates (Figure 6). There is also a close coupling between these peak detrital fluxes and a transient peak in carbonate MAR, which is exactly the coupling predicted if increased detrital accumulation is accompanied by the

20 widespread burial of organic carbon, with a resultant rapid increase in ocean pH and carbonate saturation state (Bowen and Zachos, 2010). Inverse Earth System modelling of the CIE at this location demonstrates that this interval of peak MARs (~80 to 120 ka after onset) is coincident with ~8700 Pg of carbon drawdown from the ocean-atmosphere system in the -22 ‰ $\delta^{13}C$ input and removal scenario, equivalent to ~87 % of total removal fluxes. The magnitude of increase in detrital accumulation rates at

25 the end of the event (from <6 to >8 g cm^{-2} ka^{-1}) is also of the same order as the ~40% increase in organic carbon burial rates estimated for the CIE recovery (Bowen and Zachos, 2010). Although Zumaia is a single PETM record from a single location, it has striking similarities to other Tethyan deep-water successions, such as Forada in Italy (Giusberti et al., 2016), and is likely representative of regional-scale dynamics of climate and the associated response of continental margin sedimentary

30 systems. Within the main phase of the PETM, variability within the Forada section is interpreted to be precession-paced wet and arid phases associated with a monsoonal-type subtropical climate (Giusberti et al., 2016). Measured TOC MARs through the Zumaia section are elevated during the recovery interval, ~55.83 to 55.81 Ma (Figure 6), although these data are not able to discriminate between the burial fluxes of old (pre-PETM) reworked carbon and those for newly produced (intra-PETM) organic

35 carbon – only the later will contribute to the removal of carbon from the exogenic carbon cycle. The Zumaia records cannot yet be used to trace the rates of burial of new-formed organic carbon through the PETM recovery phase, however they do provide a feasible mechanism for the timing of the recovery phase of the PETM, namely a strong precession-forcing of tropical and sub-tropical hydrological regimes and associated sediment erosion, flux and accumulation. Alongside the observed precession-

40 forced variations in sediment accumulation, there is likely a complex influence of temperature and CO_2 on the balance between rates of net primary production and organic carbon remineralization during the PETM (Cotton et al., 2015). This production / remineralization balance will control the availability of

newly formed sedimentary organic carbon for long-term burial in the sedimentary carbon sink (Cotton et al., 2015). During conditions of peak PETM warmth, enhanced organic carbon remineralization in terrestrial systems may have drastically limited the flux to continental margin systems, but with even a gradual recovery from peak-warmth conditions – forced, for example, by known enhanced carbon burial in the anoxic marine basins of the eastern Tethys during the peak-PETM (Carmichael et al., 2017) - a subtle shift in the production to respiration balance towards the availability of organic carbon for long-term burial, combined with a precession-forced peak in sediment flux and accumulation rates across terrestrial and continental margin systems, could account for the magnitude and timing of the sudden switch to widespread carbon sequestration required during the CIE recovery phase. The greatly enhanced detrital accumulation rates observed in continental margin settings such as Zumaia could also effectively mask patterns of enhanced burial of newly formed organic matter (Sluijs et al., 2014), unless the mass accumulation rates of this "new formed" organic matter can be constrained. Future studies should ~~also~~ focus on discriminating the relative contributions of this newly formed (intra-PETM) and reworked "fossil" (pre-PETM) organic carbon within these continental margin successions, as only the former will contribute to carbon sequestration.

7 Conclusions

New high-resolution stable isotopic and sediment chemistry records across the PETM interval of the Zumaia section provide new insights into the dynamics of sediment accumulation and their relationship to local climate dynamics and global carbon cycle perturbations. In comparison to deep-ocean locations, the Zumaia section has enhanced sediment accumulation rates across the critical phase of PETM onset. This provides a high-fidelity and high-resolution record of the PETM CIE that is comparable to the most complete terrestrial and marine records. The magnitude and rate of CIE onset observed at Zumaia is in close agreement with soil carbonate nodule data from the Big Horn Basin, and imply PETM onset times of less than 5000 years, with a CIE magnitude of at least ~4 ‰. Detailed correlations of existing cyclostratigraphy from the Zumaia section, together with carbon isotope stratigraphy of the CIE, to other key marine and terrestrial locations with comparable records, provides a new age model framework for the Zumaia PETM section. This age model is then used to determine detrital and carbonate mass accumulation rates through the PETM interval.

During the deposition of the characteristic PETM siliciclastic unit of Zumaia, sedimentation rates double and the mass accumulation rates of detrital sediments increase by up to four times relative to pre-event conditions. Dramatic increases in sedimentation rates during the main phase of the PETM are interpreted to represent significant changes in regional hydrology, most likely an increase in the magnitude and frequency of extreme rainfall and runoff events, potentially within an overall lower mean annual precipitation regime (Carmichael et al., 2017; Carmichael et al., 2016). These changes in sedimentation accumulation rates – and inferred perturbations to hydrology - persist throughout the PETM interval, only returning towards pre-event levels during the rapid phase of CIE recovery. This supports a close coupling between the CIE and the climate system. Peak sedimentation rates and detrital accumulation rates are observed through the recovery phase of the CIE and not the onset. We suggest

that this peak in sedimentation rates is coupled to the precession forcing of subtropical terrestrial hydrology and may provide a key to understanding the timing of the recovery phase of the CIE.

Earth System Model (cGENIE) inversion experiments, designed to replicate the observed CIE dynamics at Zumaia, reproduce an atmospheric CIE that is close to the best available terrestrial records of the CIE (Bowen et al., 2015), in timing and magnitudes. Depending on the $\delta^{13}C$ composition of the source of PETM carbon, estimated total carbon inputs during the onset of the PETM are ~3,400 Pg C (methane source, -60 ‰) or ~11,300 Pg C (organic carbon source, -22 ‰). Simulations with a silicate weathering only feedback and mechanism for carbon cycle recovery fail to reproduce the observed record in two key ways: first, they are unable to recover the coupled CIE-climate system at a rate fast enough to match the observations (<20 ka); and, second, the final sink of carbon within this feedback – marine carbonates – is isotopically too heavy to provide any significant recovery of the CIE. Simulations that match the patterns of CIE recovery require active organic or methane carbon removal, of a magnitude similar to the original carbon input. Simulations with an isotopic mismatch between source carbon (methane -60 ‰) and sink carbon (organic matter -22 ‰) require significantly more carbon removal at the end of the event than originally released during the onset. This causes a marked post event cooling of ~4 °C relative to pre-event conditions that is inconsistent with current climate records.

The results presented here demonstrate that the Earth System was capable of the sequestration of several thousand petagrams of carbon at the end of the PETM, but only after nearly one hundred thousand years within a profoundly altered climate state. The mechanism of carbon burial also appears to rely on a radical perturbation to global hydroclimates, sufficient to cause erosion and dramatically increased sediment flux rates to continental margins between three and four times pre-perturbation levels.

ACKNOWLEDGEMENTS
T.DJ acknowledges funding from a Royal Society Dorothy Hodgkin Fellowship, L.A. project CGL2014-58794-P (Spanish Ministry of Economy and Competitiveness and FEDER funds), and R.D.P. acknowledges the Royal Society Wolfson Research Merit Award. This research was supported by the Deutsche Forschungsgemeinschaft (DFG) to T.W. We would also like to thank Kernow Analytical Technology for use of the T-SEP[TM] apparatus, Victoriano Pujalte for guidance in accessing sampling sites, Enrique Cantero and Georgia Hole for assistance in sampling, and Chris Kendrick for assistance with TOC and d^{13}C$_{TOC}$ analysis. Finally, we thank Dr Ian Bull, Alison Kuhl and James Williams of the Natural Environment Research Council Life Sciences Mass Spectrometry Facility for technical assistance.

ADDITIONAL INFORMATION
Supplementary information is available in the online version of the paper. Correspondence and requests for materials should be addressed to TDJ.

References

Abdul Aziz, H., Hilgen, F. J., Van Luijk, G. M., Sluijs, A., Kraus, M. J., Pares, J. M., and Gingerich, P. D., 2008, Astronomical climate control on paleosol stacking patterns in the upper Paleocene–lower Eocene Willwood Formation, Bighorn Basin, Wyoming: Geology, v. 36, no. 7, p. 531.

Alegret, L., Matías, R., and Pérez Manuel, V., 2018, Environmental instability during the latest Paleocene at Zumaia (Basque-Cantabric Basin): The bellwether of the Paleocene-Eocene Thermal Maximum: Palaeogeography Palaeoclimatology Palaeoecology, v. 497, p. 186-200.

Alegret, L., Ortiz, S., Orue-Etxebarria, X., Bernaola, G., Baceta, J. I., Monechi, S., Apellaniz, E., and Pujalte, V., 2009, The Paleocene-Eocene Thermal Maximum: New data on microfossil turnover at the Zumaia Section, Spain: Palaios, v. 24, no. 5, p. 318-328.

Baceta, J. I., Pujalte, V., and Caballero, F., 2006, Paleocene and Early Eocene Facies and Events: a Basin-Platform-Coastal Plain Transect (South-Central and Western Pyrenees). Climate and Biota of the Early Paleogene 2006. Post Conference Field Trip Guidebook, Bilbao.

Baceta, J. I., Pujalte, V., Dinarès-Turell, J., Payros, A., Orue-Etxebarria, X., and Bernaola, G., 2000, The Paleocene/Eocene boundary interval in teh Zumaia Section (Gipuzkoa, Basque Basin): Magnetostratigraphy, and high-resolution lithostratigraphy: Revista de la Sociedad Geológica de España, v. 13, p. 375-391.

Bains, S., Corfield, R., and Norris, R., 1999, Mechanisms of climate warming at the end of the Paleocene: Science, v. 285, no. 5428, p. 724.

Bernaola, G., Baceta, J. I., Orue-Etxebarria, X., Alegret, L., Martin-Rubio, M., Arostegui, J., and Dinares-Turell, J., 2007, Evidence of an abrupt environmental disruption during the mid-Paleocene biotic event (Zumaia section, western Pyrenees): Geological Society of America Bulletin, v. 119, no. 7-8, p. 785-795.

Bowen, G. J., Maibauer, B. J., Kraus, M. J., Rohl, U., Westerhold, T., Steimke, A., Gingerich, P. D., Wing, S. L., and Clyde, W. C., 2015, Two massive, rapid releases of carbon during le onset of the Palaeocene-Eocene thermal maximum: Nature Geoscience, v. 8, no. 1, p. 44-47.

Bowen, G. J., and Zachos, J. C., 2010, Rapid carbon sequestration at the termination of the Palaeocene--Eocene Thermal Maximum: Nature Geoscience, v. 3, no. 12, p. 866-869.

Bralower, T. J., Kelly, D. C., Gibbs, S., Farley, K., Eccles, L., Lindemann, T. L., and Smith, G. J., 2014, Impact of dissolution on the sedimentary record of the Paleocene-Eocene thermal maximum: Earth and Planetary Science Letters, v. 401, p. 70-82.

Canudo, J. I., Keller, G., Molina, E., and Oritz, N., 1995, Planktic foraminiferal turnover and d13C isotopes across the Paleocene-Eocene transition at Caravaca and Zumaya, Spain: Palaeogeography Palaeoclimatology Palaeoecology, v. 114, p. 75-100.

Carmichael, M. J., Inglis, G. N., Badger, M. P. S., Naafs, B. D. A., Behrooz, L., Remmelzwaal, S., Monteiro, F. M., Rohrssen, M., Farnsworth, A., Buss, H. L., Dickson, A. J., Valdes, P. J., Lunt, D. J., and Pancost, R. D., 2017, Hydrological and associated biogeochemical consequences of rapid global warming during the Paleocene-Eocene Thermal Maximum: Global and Planetary Change, v. 157, p. 114-138.

Carmichael, M. J., Lunt, D. J., Huber, M., Heinemann, M., Kiehl, J. T., LeGrande, A., Loptson, C. A., Roberts, C. D., Sagoo, N., Shields, C., Valdes, P. J., Winguth, A., Winguth, C., and Pancost, R. D., 2016, A model-model and data-model comparison for the early Eocene hydrological cycle: Climates of the Past, v. 12, p. 455-481.

Clare, M. A., Talling, P. J., and Hunt, J. E., 2015, Implications of reduced turbidity current and landslide activity for the Initial Eocene Thermal Maximum - evidence from two distal, deep-water sites: Earth and Planetary Science Letters, v. 420, p. 102-115.

Colbourn, G., Ridgwell, A., and Lenton, T., 2013, The rock geochemical model (RokGeM) v0.9: Geoscientific Model Development, v. 6, no. 5, p. 1543-1573.

Cotton, J. M., Sheldon, N. D., Hren, M. T., and Gallagher, T. M., 2015, Positive feedback drives carbon release from soils to atmosphere during Paleocene/Eocene warming: American Journal of Science, v. 315, no. 4, p. 337-361.

Cui, Y., Kump, L. R., Ridgwell, A. J., Charles, A. J., Junium, C. K., Diefendorf, A. F., Freeman, K. H., Urban, N. M., and Harding, I. C., 2011, Slow release of fossil carbon during the Palaeocene--Eocene Thermal Maximum: Nature Geoscience, v. 4, no. 7, p. 481-485.

Dickens, G. R., O'Neil, J. R., Rea, D. K., and Owen, R. M., 1995, Dissociation of oceanic methane hydrate as a cause of the carbon isotope excursion at the end of the Paleocene: Paleoceanography, v. 10, no. 6, p. 965-971.

Dinarès-Turell, J., Baceta, J., Bernaola, G., Orue-Etxebarria, X., and Pujalte, V., 2007, Closing the Mid-Palaeocene gap: Toward a complete astronomically tuned Palaeocene Epoch and Selandian and Thanetian GSSPs at Zumaia (Basque Basin, W Pyrenees): Earth and planetary science letters, v. 262, no. 3-4, p. 450-467.

Dinarès-Turell, J., Baceta, J. I., Pujalte, V., Orue-Etxebarria, X., and Bernaola, G., 2002, Magnetostratigraphic and cyclostratigraphic calibration of a prospective Palaeocene/Eocene stratotype at Zumaia (Basque Basin, northern Spain): Terra Nova, v. 14, no. 5, p. 371-378.

Dinarès-Turell, J., Baceta, J. I., Pujalte, V., Orue-Etxebarria, X., Bernaola, G., and Lorito, S., 2003, Untangling the Palaeocene climatic rhythm: an astronimically calibrated Early Palaeocene magnetostratigraphy and biostratigraphy at Zumaia (Basque basin, northern Spain): Earth and Planetary Science Letters, v. 216, p. 483-500.

Dunkley Jones, T., Lunt, D. J., Schmidt, D. N., Ridgwell, A., Sluijs, A., Valdes, P. J., and Maslin, M., 2013, Climate model and proxy data constraints on ocean warming across the Paleocene/Eocene Thermal Maximum: Earth-Science Reviews, v. 125, no. 0, p. 123-145.

Gavrilov, Y. O., Kodina, L., Lubchenko, I., and Muzylev, N., 1997, The late Paleocene anoxic event in epicontinental seas of the Peri-Tethys and formation of the sapropelite unit: Sedimentology and geochemistry: Lithology and Mineral Resources, v. 32, p. 427-450.

Giusberti, L., Galazzo, F. B., and Thomas, E., 2016, Variability in climate and productivity during the Paleocene-Eocene Thermal Maximum in the western Tethys (Forada section): Climate of the Past, v. 12, no. 2, p. 213-240.

Gutjahr, M., Ridgwell, A., Sexton, P. F., Anagnostou, E., Pearson, P. N., Pälike, H., Norris, R. D., Thomas, E., and Foster, G. L., 2017, Very large release of mostly volcanic carbon during the Palaeocene-Eocene Thermal Maximum: Nature, v. 548, p. 573-577.

John, C. M., Bohaty, S. M., Zachos, J. C., Sluijs, A., Gibbs, S., Brinkhuis, H., and Bralower, T. J., 2008, North American continental margin records of the Paleocene-Eocene thermal maximum: Implications for global carbon and hydrological cycling: Paleoceanography, v. 23, p. doi:10.1029/2007PA001465.

Kirtland Turner, S., and Ridgwell, A., 2016, Development of a novel empirical framework for interpreting geological carbon isotope excursions, with implications for the rate of carbon injection across the PETM: Earth and Planetary Science Letters, v. 435, p. 1-13.

Manners, H. R., Grimes, S., Sutton, P. A., Domingo, L., Leng, M. J., Twitchett, R. T., Hart, M. B., Dunkley Jones, T., Pancost, R. D., Duller, R., and Lopez-Martinez, N., 2013, Magnitude and profile of organic carbon isotope records from the Palaeocene-Eocene Thermal Maximum: evidence from northern Spain: Earth and Planetary Science Letters, v. 377, p. 220-230.

McCarren, H., Thomas, E., Hasegawa, T., Röhl, U., and Zachos, J. C., 2008, Depth dependency of the Paleocene-Eocene carbon isotope excursion: Paired benthic and terrestrial biomarker records (Ocean Drilling Program Leg 208, Walvis Ridge): Geochemistry Geophysics Geosystems, v. 9, no. 10, p. doi:10.1029/2008GC002116.

McInerney, F. A., and Wing, S. L., 2011, The Paleocene-Eocene Thermal Maximum: A perturbation of carbon cycle, climate, and biosphere with implications for the future: Annual Review of Earth and Planetary Sciences.

Meissner, K. J., Bralower, T., Alexander, K., Dunkley Jones, T., Sijp, W., and Ward, M., 2014, The Paleocene-Eocene Thermal Maximum: How much carbon is enough?: Paleoceanography, v. 29, p. 946-963.

Murphy, B. H., Farley, K. A., and Zachos, J. C., 2010, An extraterrestrial 3He-based timescale for the Paleocene-Eocene thermal maximum (PETM) from the Walvis Ridge, IODP Site 1266: Geochemica et Cosmochemica Acta, v. 74, p. 5098-5108.

Panchuk, K., Ridgwell, A., and Kump, L., 2008, Sedimentary response to Paleocene-Eocene Thermal Maximum carbon release: A model-data comparison: Geology, v. 36, no. 4, p. 315.

Penman, D. E., 2016, Silicate weathering and North Atlantic silica burial during the Paleocene-Eocene Thermal Maximum: Geology, v. 44, no. 9, p. 731-734.

Penman, D. E., Turner, S. K., Sexton, P. F., Norris, R. D., Dickson, A. J., Boulila, S., Ridgwell, A., Zeebe, R. E., Zachos, J. C., Cameron, A., Westerhold, T., and Röhl, U., 2016, An abyssal carbonate compensation depth overshoot in the aftermath of the Palaeocene-Eocene Thermal Maximum: Nature Geoscience, v. 9, no. 8, p. 575-+.

Pujalte, V., Baceta, J. I., and Schmitz, B., 2015, A massive input of coarse-grained siliciclastics in the Pyrenean Basin during the PETM: the missing ingredient in a coeval abrupt change in hydrological regime: Climate of the Past, v. 11, no. 12, p. 1653-1672.

Ridgwell, A., and Schmidt, D. N., 2010, Past constraints on the vulnerability of marine calcifiers to massive carbon dioxide release: Nature Geoscience, v. 3, no. 3, p. 1-5.

Röhl, U., Westerhold, T., Bralower, T., and Zachos, J., 2007, On the duration of the Paleocene-Eocene thermal maximum (PETM): Geochemistry, Geophysics, Geosystems, v. 8, no. 12, p. 1-13.

Schmitz, B., Asaro, F., Molina, E., Monechi, S., Salis, K. v., and Speijer, R. P., 1997, High-resolution iridium, d13C, d18O, foraminifera and nannofossil profiles across the latest Paleocene benthic extinction event at Zumaya: Palaeogeography Palaeoclimatology Palaeoecology, v. 133, p. 49-68.

Schmitz, B., and Pujalte, V., 2007, Abrupt increase in seasonal extreme precipitation at the Paleocene-Eocene boundary: Geology, v. 35, no. 3, p. 215-218.

Schmitz, B., Pujalte, V., and Nunez-Betelu, K., 2001, Climate and sea-level perturbations during the Initial Eocene Thermal Maximum: evidence from siliciclastic units in the Basque Basin (Ermua, Zumaia and Trabakua Pass), northern Spain: Palaeogeography Palaeoclimatology Palaeoecology, v. 165, no. 3-4, p. 299-320.

Short, D. A., Mengel, J. G., Crowley, T. J., Hyde, W., and North, G. R., 1991, Filtering of Milankovitch Cycles by Earth's Geography: Quaternary Research, v. 35, p. 157-173.

Sluijs, A., Bowen, G. J., Brinkhuis, H., Lourens, L. J., and Thomas, E., 2007, The Palaeocene-Eocene Thermal Maximum super greenhouse: biotic and geochemical signatures, age models and mechanisms of global change, in Williams, M., Haywood, A. M., Gregory, J., and Schmidt, D. N., eds., Deep-time perspectives on climate change: Marrying the signal from computer models and biological proxies: London, The Micropalaeontological Society Special Publication, p. 323-350.

Sluijs, A., van Roij, L., Harrington, G. J., Schouten, S., Sessa, J. A., Levay, L. J., Reichart, G. J., and Slomp, C. P., 2014, Warming, euxinia and sea level rise during the Paleocene-Eocene Thermal Maximum on the Gulf Coastal Plain: implications for ocean oxygenation and nutrient cycling: Climate of the Past, v. 10, no. 4, p. 1421-1439.

Storme, J.-Y., Devleeschouwer, X., Schnyder, J., Cambier, G., Baceta, J. I., Pujalte, V., Di Matteo, A., Iacumin, P., and Yans, J., 2012, The Palaeocene/Eocene boundary section at Zumaia (Basque-Cantabric Basin) revisited: new insights from high-resolution magnetic susceptibility and carbon isotope chemostratigraphy on organic matter (δ13Corg): Terra Nova, v. 00, p. 1-9.

Svensen, H., Planke, S., Malthe-Sorenssen, A., Jamtveit, B., Myklebust, R., Eidem, T., and Rey, S., 2004, Release of methane from a volcanic basin as a mechanism for initial Eocene global warming: Nature, v. 429, no. 6991, p. 542-545.

Westerhold, T., Röhl, U., Laskar, J., Raffi, I., Bowles, J., Lourens, L., and Zachos, J., 2007, On the duration of magnetochrons C24r and C25n and the timing of early Eocene global warming events: Implications from the Ocean Drilling Program Leg 208 Walvis Ridge depth transect: Paleoceanography, v. 22, no. 2.

Westerhold, T., Röhl, U., Pälike, H., Wilkens, R., Wilson, P. A., and Acton, G., 2014, Orbitally tuned timescale and astronomical forcing in the middle Eocene to early Oligocene: Climates of the Past, v. 10, p. 955-973.

Westerhold, T., Röhl, U., Raffi, I., Fornaciari, E., Monechi, S., Reale, V., Bowles, J., and Evans, H. F., 2008, Astronomical calibration of the Paleocene time: Palaeogeography Palaeoclimatology Palaeoecology, v. 257, no. 4, p. 377-403.

Westerhold, T., Röhl, U., Wilkens, R. H., Gingerich, P. D., Clyde, W. C., Wing, S. L., Bowen, G. J., and Kraus, M. J., 2018, Synchronizing early Eocene deep-sea and continental records – cyclostratigraphic age models for the Bighorn Basin Coring Project drill cores: Climates of the Past, v. 14, p. 303-319.

5 Willmott, V., Rampen, S., Domack, E., Canals, M., Sinninghe Damste, J. S., and Schouten, S., 2009, Holocene changes in Proboscia diatom productivity in shelf waters of the north-western Antarctic Peninsula: Antarctic Science, v. 22, no. 1, p. 3-10.

Zachos, J. C., Mccarren, H., Murphy, B., Röhl, U., and Westerhold, T., 2010, Tempo and scale of late Paleocene and early Eocene carbon isotope cycles: Implications for the origin of hyperthermals: Earth
10 and planetary science letters, v. 299, no. 1-2, p. 242-249.

Zachos, J. C., Röhl, U., Schellenberg, S. A., Sluijs, A., Hodell, D. A., Kelly, D. C., Thomas, E., Nicolo, M., Raffi, I., Lourens, L. J., McCarren, H., and Kroon, D., 2005, Rapid acidification of the ocean during the Paleocene-Eocene thermal maximum: Science, v. 308, no. 5728, p. 1611-1615.

Zeebe, R. E., Ridgwell, A., and Zachos, J. C., 2016, Anthropogenic carbon release rate unprecedented
15 during the past 66 million years: Nature Geoscience, v. 9, p. 325-329.

Zeebe, R. E., Zachos, J. C., and Dickens, G. R., 2009, Carbon dioxide forcing alone insufficient to explain Palaeocene-Eocene Thermal Maximum warming: Nature Geoscience, v. 2, no. 8, p. 576-580.

Table 1. Summary details of cGENIE simulations detailing isotopic compositions of source carbon - input during the onset of the PETM to match Zumaia CIE profile – and the nature of modelled CIE recovery, whether by silicate weathering only (Experiment 1), or by active carbon removal. The isotopic composition of this carbon removal ("Sink") is also listed. Net C fluxes are calculated by the model to match the CIE profile and do not include carbon removed through silicate weathering.

Experiment	$\delta^{13}C$ composition		Net C flux (PgC)			Average Emission Rates (Pg C yr^{-1})	
	Source	Sink	0 to 19 ka	19 to 78 ka	>78 ka	0 to 19 ka	19 to 78 ka
1. Mixed source; silicate weathering	–22 ‰	Carbonate burial	+11376	+1809	0	0.60	0.03
2. Mixed source; terrestrial carbon burial	–22 ‰	–22 ‰ (C_{org})	+11316	+1809	-10083	0.60	0.03
3. Methane source; methane removal	–60 ‰	–60 ‰ (CH_4)	+3382	+772	-3244	0.18	0.01
4. Methane source; terrestrial carbon burial	–60 ‰	–22 ‰ (C_{org})	+3483	+2360	-8640	0.18	0.04
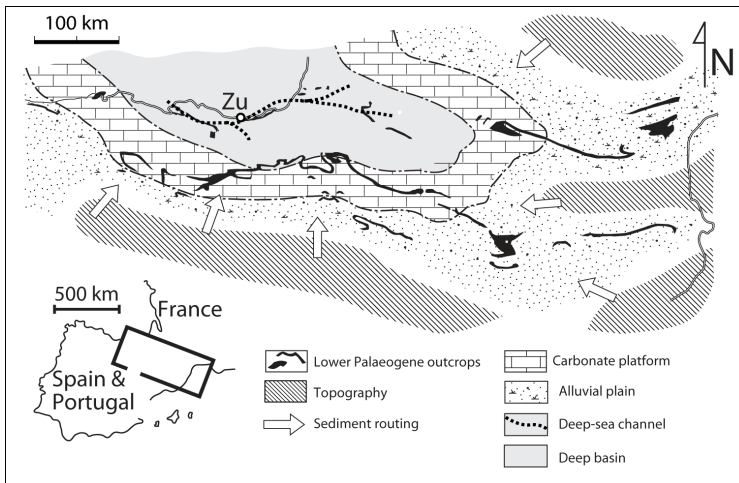
Figure 1: Location of Zumaia section and relationship to the terrestrial and shallow shelf carbonate depositional environments; after Pujalte et al. (2015).
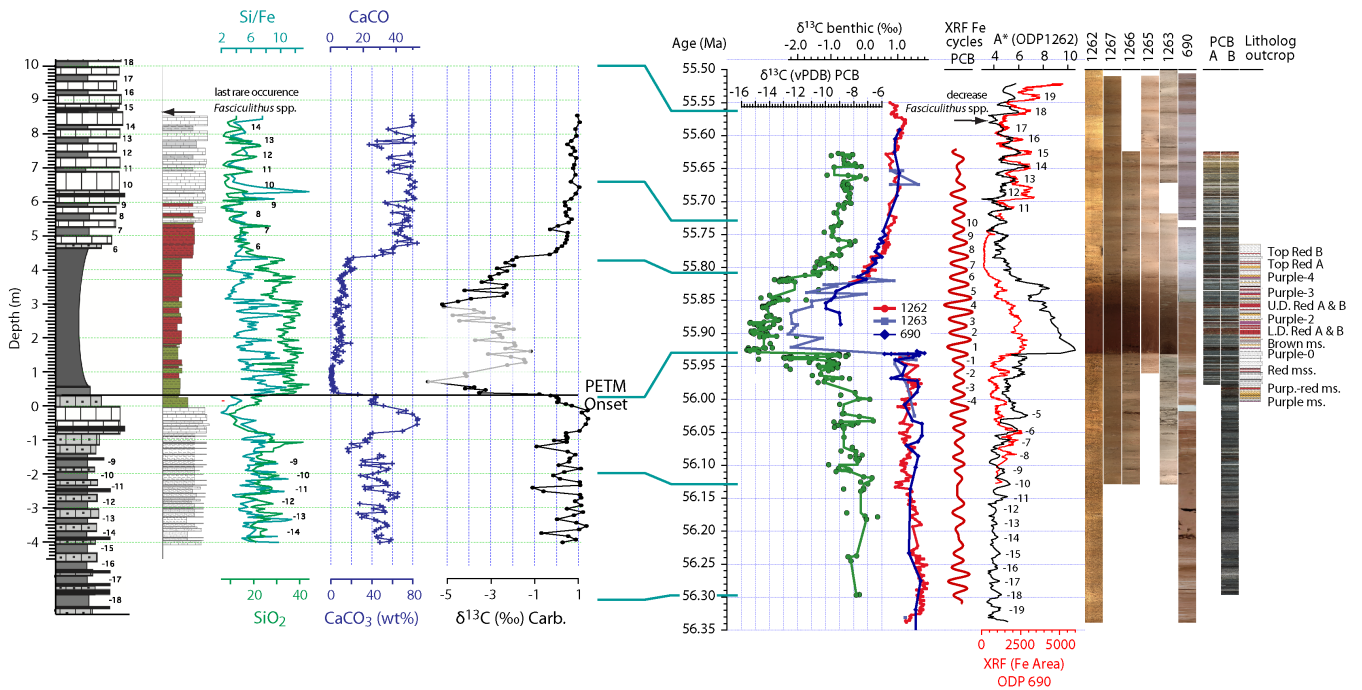
Figure 2. New sediment geochemistry data for the Zumaia section and correlation to existing deep ocean and terrestrial records (inter-site correlations and age model of Westerhold et al. 2018). Left hand panel against depth in the Zumaia section, from left to right: lithological log after Storme et al. (20120); lithological log produced during sample collection for this study (2011); SiO₂ weight percent and Si/Fe ratio based on weight percents of oxides (SiO₂/Fe₂O₃) from bulk sediment XRF analyses, pre-PETM and post-PETM precession cycles numbered in black; weight percent CaO and CaCO₃ from XRF; new bulk carbonate δ¹³C (this study). Right hand panel, against age (Westerhold et al. 2018), from left to right: Polecat Bench Core (PCB) soil carbonate nodule δ¹³C (green; Bown et al. 2015); deep ocean benthic foraminiferal δ¹³C (Bains et al., 1999; McCarren et al., 2008); Gaussian filter of the longer 8.2 m cycle (precession) of the Fe data from PCB-B (red; Westerhold et al. 2018); ODP Site 690 XRF core scanning Fe data in red, ODP Site 1262 A* colour reflectance data in black; composite core section photos from deep ocean sites ODP 1262, 1267, 1266, 1265, 1263 and 690 and terrestrial PCB sites A and B, with the later correlated to nearby outcrop lithologies (Westerhold et al. 2018).
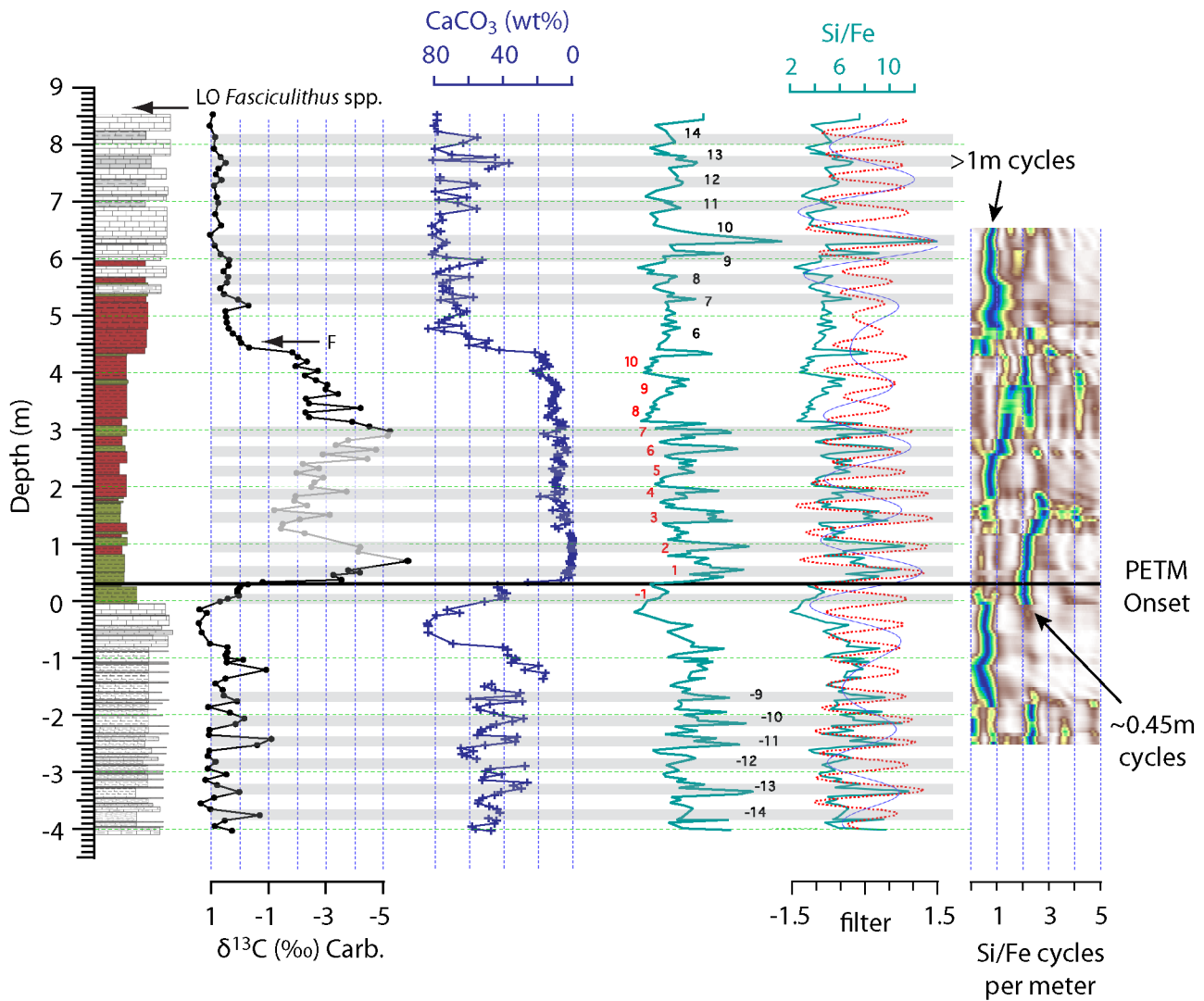
Figure 3. New sediment geochemistry data for the Zumaia section. From left to right: lithological log produced during sample collection for this study (2011); bulk carbonate δ¹³C; weight percent CaO and CaCO₃ from bulk sediment XRF analyses; SiO₂ weight percent and Si/Fe ratio based on weight percents of oxides (SiO₂/Fe₂O₃) from bulk sediment XRF analyses, pre-PETM and post-PETM precession cycles numbered in black, intra-PETM ~~half-precession~~ cycles numbered in red; Si/Fe ratios with Gaussian filters of the dominant cycles 0.45m (red) and 1m (blue); evolutive spectral analysis for Si/Fe.
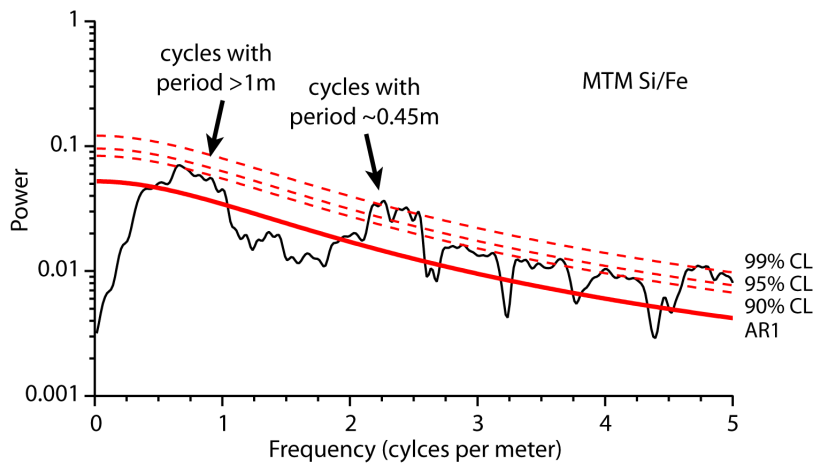
Figure 4. MTM power spectra for Si/Fe ratios; highlighted are spectral peaks equivalent to cycles with period >1 m and ~0.45 m.

30
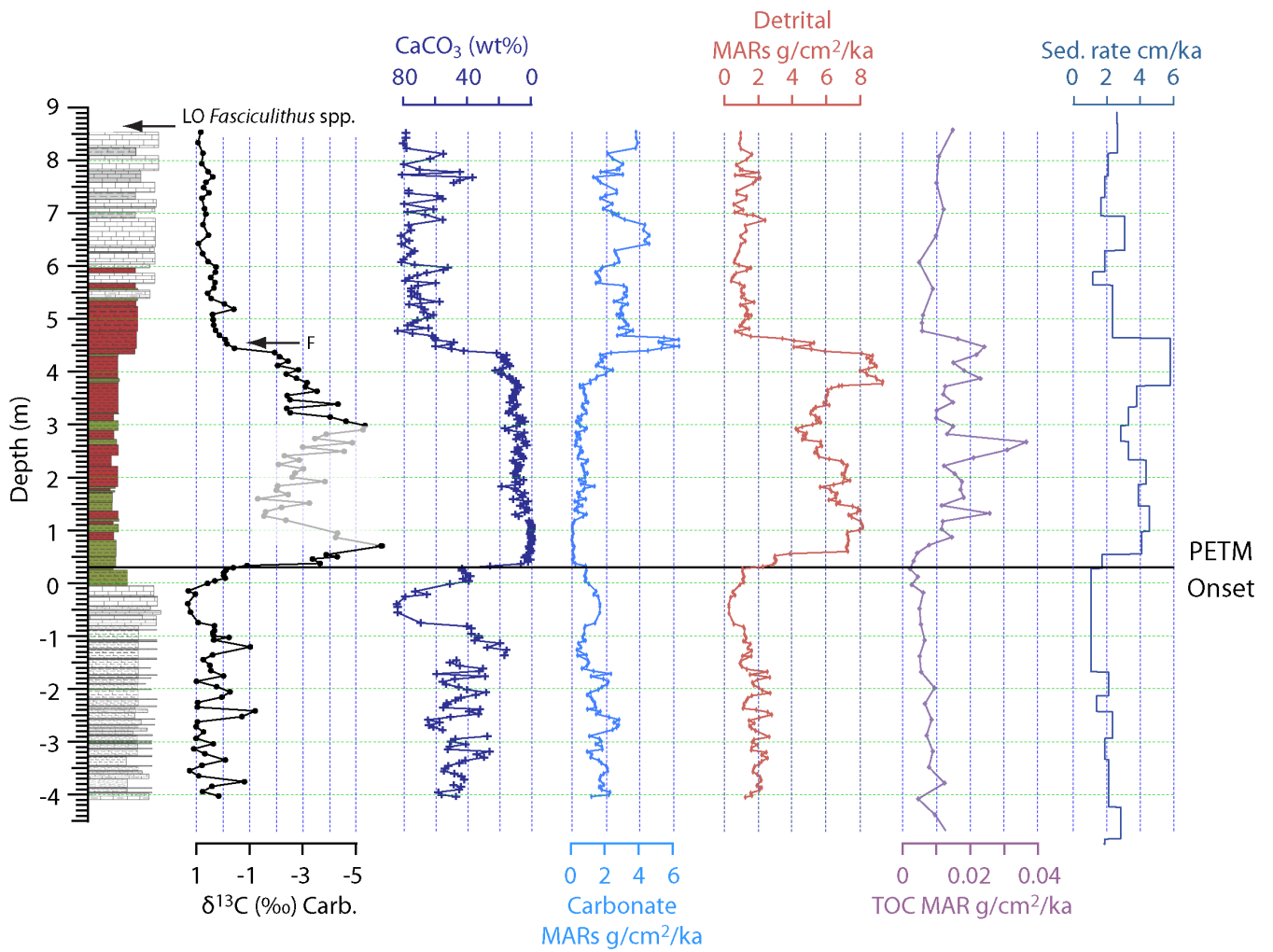
Figure 5. New carbonate, detrital and organic carbon mass accumulation and sedimentation rates for the Zumaia section. From left to right: lithological log produced during sample collection for this study (2011); bulk carbonate δ¹³C; weight percent CaCO₃ derived from XRF CaCO calibrated to discrete CaCO₃ analyses (see methods); CaCO₃ mass accumulation rate (light blue); detrital mass accumulation rate (red); organic carbon accumulation rate (purple); and, linear sedimentation rates (far right) derived from the new cyclostratigraphic framework.
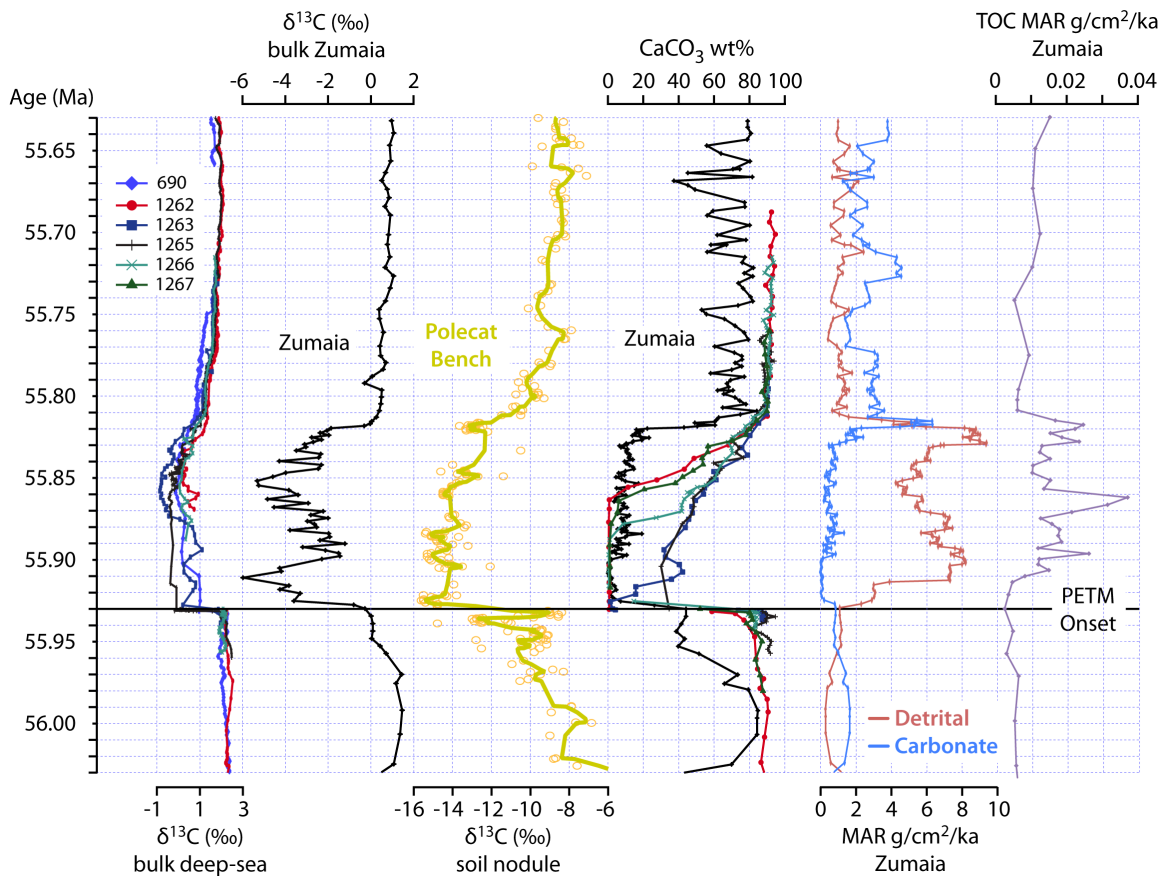
Figure 6. Comparison of the Zumaia records against terrestrial (Big Horn Basin) and deep-ocean sites (Walvis Ridge, ODP Sites 1262, 1263, 1265, 1266, 1267; Maud Rise ODP Site 690) on the same cyclostratigraphic age model. From left to right: bulk carbonate δ13C for deep ocean sites; bulk carbonate δ13C for Zumaia; soil nodule δ13C from the Big Horn Basin; CaCO₃ records from Zumaia and the deep-ocean sites; detrital (red), CaCO₃ (blue) and organic carbon (purple, far left) mass accumulation rates from Zumaia.
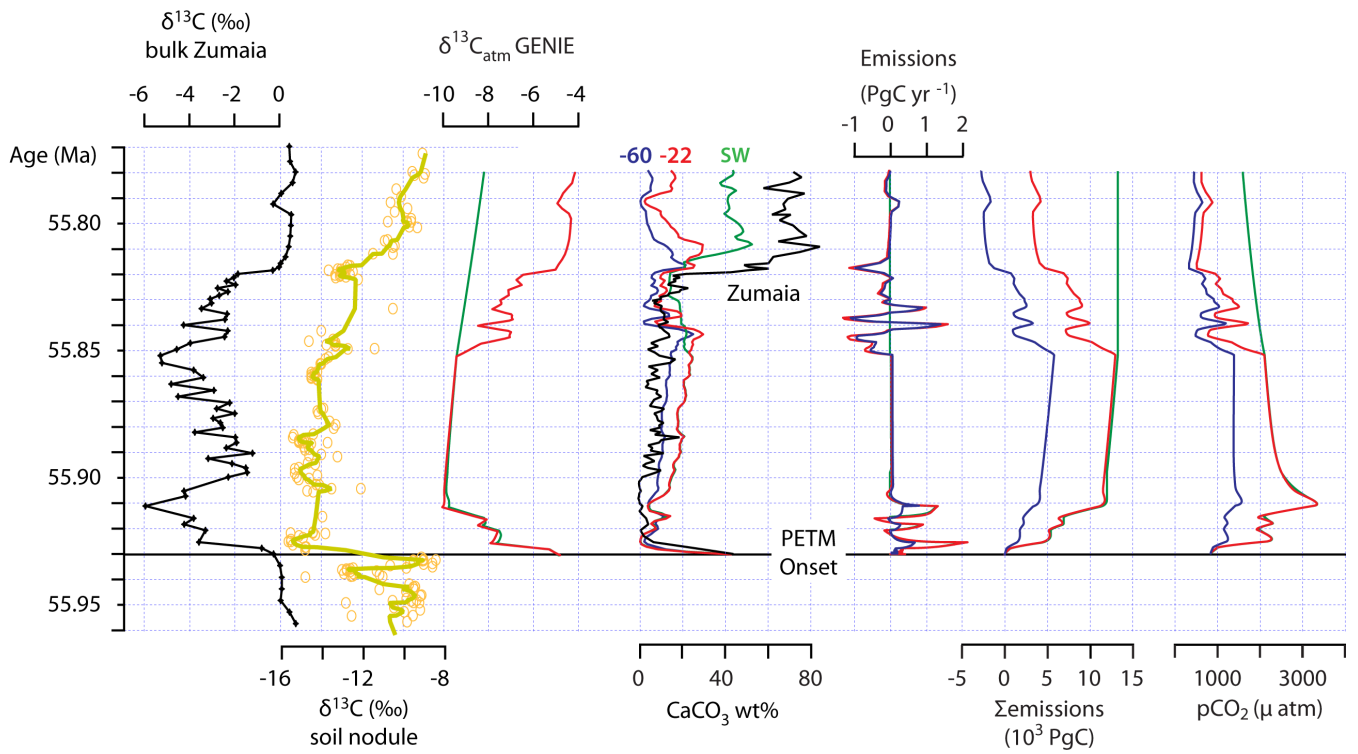
Figure 7. Results of inverse modelling with cGENIE Earth System Model. From left to right: the bulk carbonate δ¹³C for Zumaia which drives model inversions (black); soil nodule δ¹³C record of the Big Horn Basin (yellow), as representative of atmospheric CO₂ δ¹³C for comparison to model results; modelled δ¹³C composition of atmospheric carbon dioxide; carbon emission rate in PgC per year; cumulative carbon emissions (cumulative input minus removal); modelled atmospheric pCO₂; modelled and actual weight % CaCO₃ content of the sediment column at Zumaia; modelled carbon emission and removal rates; cumulative modelled carbon emissions / removal; modelled atmospheric pCO₂. The model scenarios are as follows: 1) carbon input at δ¹³C of -22 ‰ during the onset, no carbon removal (green); 2) carbon input and removal with δ¹³C of -22 ‰ to follow Zumaia target CIE (red); 3) carbon input with δ¹³C of -60 ‰ and removal of carbon with δ¹³C of -22 ‰ to follow Zumaia target CIE (blue). All simulations have active temperature-dependent silicate weathering feedbacks operative throughout.